Journal of Aerosol Science 151 (2021) 105652

Contents lists available at ScienceDirect

Journal of Aerosol Science

journal homepage: http://www.elsevier.com/locate/jaerosci

Nanoparticle gas phase electrodeposition: Fundamentals, fluid dynamics, and deposition kinetics

Leslie Schlag [a], Nishchay A. Isaac [a], Helene Nahrstedt [a], Johannes Reiprich [a], Adriana Ispas [b], Thomas Stauden [a], Jörg Pezoldt [a], Andreas Bund [b], Heiko O. Jacobs [a,*]

[a] Fachgebiet Nanotechnologie, Technische Universität Ilmenau, Gustav-Kirchhoff-Straße 1, 98693, Ilmenau, Germany
[b] Fachgebiet Elektrochemie und Galvanotechnik, Technische Universität Ilmenau, Gustav-Kirchhoff-Straße 6, 98693, Ilmenau, Germany

ARTICLE INFO

Keywords:
Spark discharge
Langmuir probe
Debye length
Nanoparticle formation and transport
Thin film deposition

ABSTRACT

This communication uncovers missing fundamental elements and an expanded model of gas phase electrodeposition; a relatively new and in large parts unexplored process, which combines particle generation, transport zone and deposition zone in an interacting setup. The process enables selected area deposition of charged nanoparticles that are dispersed and transported by a carrier gas at atmospheric pressure conditions. Two key parameters have been identified: carrier gas flow rate and spark discharge power. Both parameters affect electrical current carried by charged species, nanoparticle mass, particle size and film morphology. In combination, these values enable to provide an estimate of the gas flow dependent Debye length. Together with Langmuir probe measurements of electric potential and field distribution, the transport can be described and understood. First, the transport of the charged species is dominated by the carrier gas flow. In close proximity, the transport is electric field driven. The transition region is not fixed and correlates with the electric potential profile, which is strongly dependent on the deposition rate. Considering the film morphology, the power of the discharge turns out to be the most relevant parameter. Low spark power combined with low gas flow leads to dendritic film growth. In contrast, higher spark power combined with higher gas flow produces compact layers.

1. Introduction

Gas phase electrodeposition is an emerging deposition process, which enables the selected area deposition of electrically charged particles under atmospheric pressure conditions (H. O. Jacobs, 2001; Heiko O. Jacobs, Campbell, & Steward, 2002). As a brief introduction, the term "gas-phase electrodeposition", is commonly used to point out commonalties with "liquid-phase wet chemical electrodeposition". The common feature is that charged particles are transported to biased surfaces to be neutralized to build up metallic (Barry, Steward, Lwin, & Jacobs, 2003) or semiconducting (Binions & Naik, 2013; Cole, Lin, Barry, & Jacobs, 2009) film structures. However, it is a dry process. The liquid is replaced by a carrier gas. Moreover, the particles are not atomic ions but charged nanoparticles (typically < 10 nm) or charged molecules. Finally, the origin of the charged species can be more versatile. For example, in combination with a corona charger (Fang et al., 2014b) nearly any particle source including sources that release small molecules can

* Corresponding author.
E-mail address: heiko.jacobs@tu-ilmenau.de (H.O. Jacobs).

https://doi.org/10.1016/j.jaerosci.2020.105652
Received 30 March 2020; Received in revised form 18 August 2020; Accepted 19 August 2020
Available online 1 September 2020

be used to produce a flux of electrically charged spices, and several reports have shown this possibility (Fang et al., 2014b; Lin, Fang, Park, Johnson, & Jacobs, 2013a; Lin, Fang, Park, Stauden, et al., 2013b; Reiprich et al., 2018). Considering inorganic nanoparticles, the use of spark discharge based plasmas (Byeon, Park, & Hwang, 2008; Cole et al., 2009; Feng, Hontañón, et al., 2016a; Hou, Kondoh, Ohta, & Gao, 2005; Messing, Dick, Wallenberg, & Deppert, 2009; Park et al., 2000; Schütze et al., 1998; Tabrizi, Ullmann, Vons, Lafont, & Schmidt-Ott, 2009; Tendero, Tixier, Tristant, Desmaison, & Leprince, 2006) has proven to be a successful approach to produce < 5 nm sized particles which are charged. Spark discharge is used as a method to produce pure metals, metal oxide nanomaterials by various research groups. It is an upcoming technique with applications in catalysis (Messing et al., 2010), hydrogen storage (Vons, Leegwater, Legerstee, Eijt, & Schmidt-Ott, 2010), functional nanoalloys (Feng, Ramlawi, Biskos, & Schmidt-Ott, 2018), environmental studies (Kuznetsov, Rakhmanova, Popovicheva, & Shonija, 2003), textile industry (Feng, 2017), medical studies (Bitterle et al., 2006),

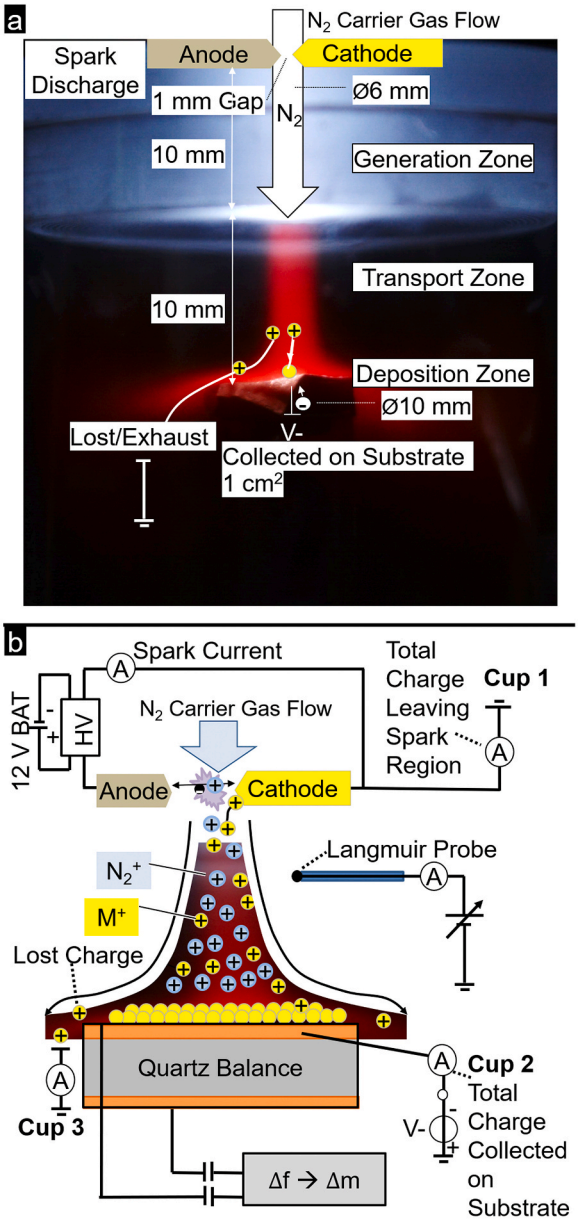

Fig. 1. Photograph of the utilized gas phase electrodeposition test platform next to schematics highlighting directly measurable key quantities of the process. (a) The photograph depicts three regions: generation zone, transport zone, and deposition zone. (b) The schematic details circuit diagrams, locations of Faraday cups (cups 1–3), a quartz balance, and a Langmuir probe to record carrier gas flow dependent values; specifically, the (i) current leaving the spark region (cup 1), (ii) current collected on the substrate (cup 2), (iii) spilled current into the exhaust (cup 3), (iv) change of mass on the substrate as a result of collected particles, and (v) electric potential profile along the trajectory.

and magnetic nanomaterials (Sabzehparvar, Kiani, & Tabrizi, 2018). Charged nanoparticles produced as an aerosol via spark discharge can be deposited onto a substrate using electrostatic precipitator (Preger, Overgaard, Messing, & Magnusson, 2020), localized deposition can be attained with nanopatterning conducting substrates (Fang et al., 2016), high throughput in deposition of semi-conducting metal oxides is possible using inertial impaction (Isaac, Valenti, Schmidt-Ott, & Biskos, 2016). The deposition technique is governed by the application.

At present, the described process has been applied in various areas. As an atmospheric pressure deposition process, it has been used to deposit patterned films (Cole, Wang, Knuesel, & Jacobs, 2008), rod like structures (Lin, Cole, & Jacobs, 2010), 3D self-aligning interconnects (Fang et al., 2016), and other two- and three-dimensional shaped structures (Cole et al., 2009). With the exception of four reports that deposited structures composed of organic particles including proteins and bacteria (Fang et al., 2014b, 2014a; Lin, Fang, Park, Johnson, & Jacobs, 2013a; Reiprich et al., 2018) the reported films and patterned 3D structures were composed primarily of inorganic metallic (Cole, Lin, Barry, & Jacobs, 2010; Lin et al., 2010) and semiconducting (Cole et al., 2009) nanoparticles. Demonstrated applications include the printing of 3D shaped metallic electrodes for solar cells (Cole et al., 2010; Lin et al., 2010), the collection of nanoparticle leading to the growth of electrically conductive point-to-point self-aligned nanobridge based interconnects (Fang et al., 2016), and the printing of 3D shaped SERS based sensors (Jung et al., 2014; Lin, Fang, Park, Johnson, & Jacobs, 2013b; Lin, Fang, Park, Stauden, et al., 2013a). More remote areas include the utilization as a localized collection method of toxic analytes, which are electrically charged, to enable localized collection and to increase the concentration and response time of various sensing concepts that require the analyte to deposit on a surface (Fang et al., 2014b, 2014a; Lin, Fang, Park, Johnson, & Jacobs, 2013b).

In addition to the large number of applications, there are already a number of studies on the simulation of one-step aerosol synthesis of nanoparticle agglomerate films (Mädler, Lall, & Friedlander, 2006), the relationship between particle deposition characteristics and the mechanism of particle arrival (Rodríguez-Pérez, Castillo, & Antoranz, 2005), and porous particulate film depositions in the transition regime (Lindquist, Pui, & Hogan, 2014). Experiments were also carried out to deposit particles in layers, to gain knowledge about the structure of deposits formed from electrosprayed aggregates of nanoparticles (Castillo, Martin, Rodriguez-Perez, Higuera, & Garcia-Ybarra, 2018; Higuera, 2018; Tang & Gomez, 2017). These experiments used titania particles, which lead to strong dendrite growth due to their oxide shell. A similar approach was also used for a deposition map to find coating process regimes of 20 nm silica nanoparticles (Brewer, Shibuta, Francis, Kumar, & Tsapatsis, 2011). Other modelling attempts focused on the capturing mechanism (referred to as deposition zone) using a charge dissipating conductor underneath a patterned insulator with small pore like openings. The formation of desired 3D shapes that grew out of the charge dissipating openings under the influence of the dynamic evolving funnel-like electric field, was the main focus in previous simulation models (Bae, Pikhitsa, Cho, & Choi, 2017; Cole et al., 2009; Ha et al., 2014). Numerical studies of the controlled electrodeposition of charged nanoparticles in an electric field (Rusinque, Fedianina, Weber, & Brenner, 2019) have been of interest in the recent past.

However, the process of gas phase electrodeposition is more involved and should be considered as a system that is composed of three spatially separated but interacting zones: the particle generation zone, the transport zone, and the deposition zone. Prior studies focused on either the particle generation or particle deposition zones. Moreover, actual values of the gas ion concentration, potential distribution, particle flux have not yet been reported. They are critical to establish the mass transport and other parameters such as the Debye screening length, which has only been estimated with high error margins (Barry & Jacobs, 2006).

To alleviate this high level of uncertainty, this study reports the direct measurement of relevant physical quantities. Specifically, Faraday cup, Langmuir probe, and quartz balance measurements are conducted in various regions in the reactor to monitor the (i) electrical current carried by the charged nanoparticles and gas ions, the (ii) electrical potential distribution, and the (iii) mass collection rate deposited on the substrate. The measurements are used in combination with the Nernst-Planck equation to develop a semi-empirical model of the transport. It enables the identification of two different transport regions, referred to as (iv) “carrier gas dominated mass transport” and (v) “electric field dominated mass transport”, the calculation of the (vi) ratio between charged nanoparticles and charged gas ions, and (vii) Debye screening length. Moreover, two key process parameters were identified, which impact most of the above-mentioned values by several orders of magnitude, in particular the carrier gas flow rate and power of the spark discharge-based plasma. This two-dimensional parameter space enables a tailored adjustment of the film morphology.

2. Material and methods

Fig. 1 provides a photograph of the utilized gas phase electrodeposition test platform next to schematics highlighting directly measurable key quantities to gain a deeper understanding of the process. The two adjustable key parameters are the carrier gas flow rate and the power of the spark discharge-based plasma that is utilized to produce a flux of charged particles. Both parameters effect measurable quantities such as the electrical current carried by the charged nanoparticles and gas ions, the nanoparticle mass, and particle size. It is first described in fairly general terms before we detail the measurements to extract the relevant physical parameters to establish a model of the transport and deposition process.

The photograph (Fig. 1a) depicts three regions, the generation zone, the transport zone, and the deposition zone. In the generation zone an inert gas flows through a spark discharge between two consumable metallic electrodes, which operate at a typical gap distance of 1 mm and $+V = 1000$ V electrode voltage. The electrode metal purity is 99.999%. The high voltage is converted from a 12 V car battery with a Gamma High Voltage block MC50R to 0.5–5 kV. The spark voltage was measured with a 1000:1 Fluke converter connected with a conventional Fluke 87 RMS Multimeter. The charging of the gas molecules in the electrical field between the electrodes leads to ionization processes, which move the positive gas ions to the cathode. There, the gas ions collide and remove metallic clusters by cathode erosion. These clusters are transported away by the inert gas flow and form a mixture of charged gas ions (predominantly positive) and charged nanoparticles (predominantly positive). Subsequently, the nanoparticles are transported by a

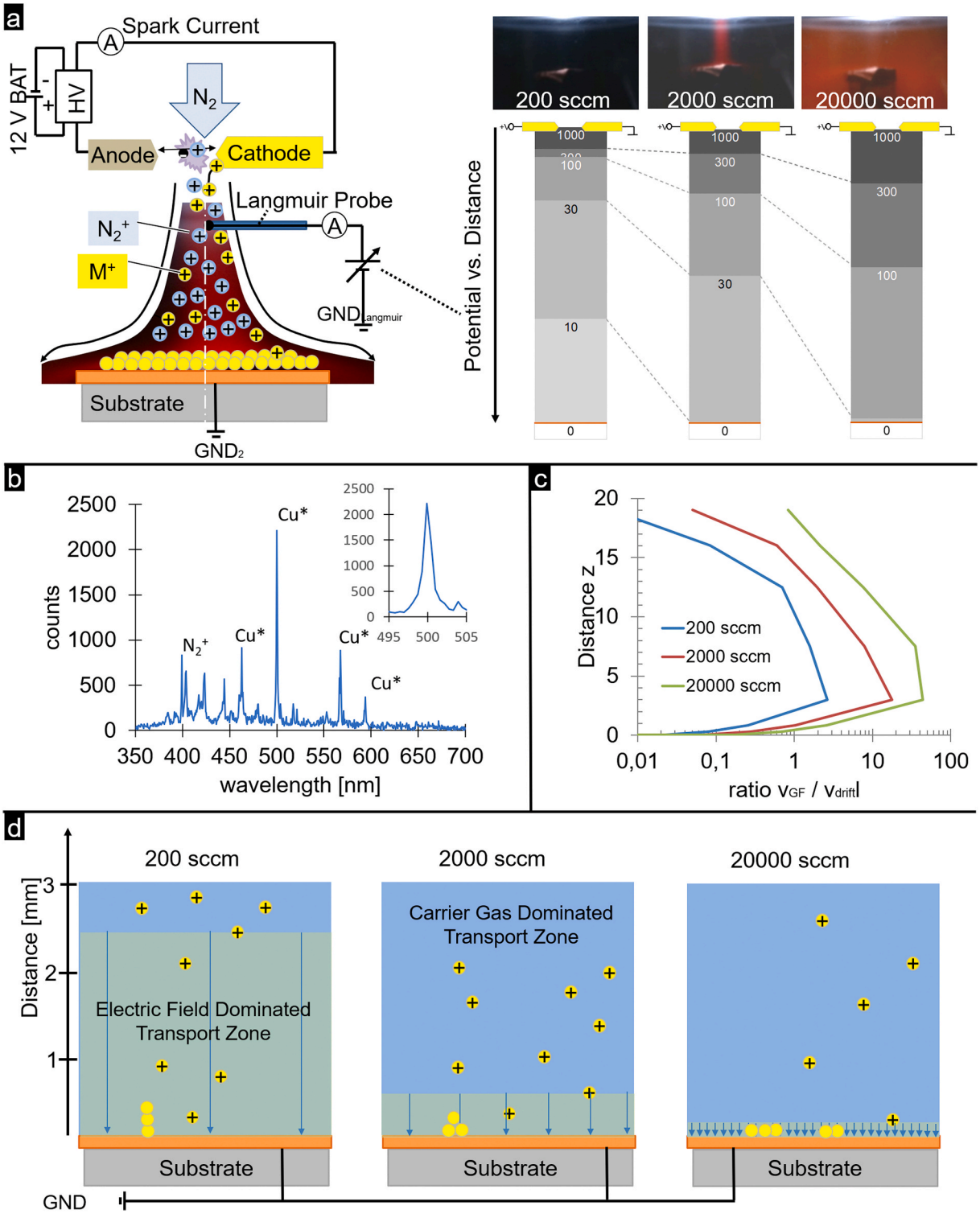

Fig. 2. Results of the optical emission, the electric potential profiles as a function of the carrier gas flow, the OES spectrum at 2000 sccm gas flow rate, and the crossover between the identified transport zones. (a) Schematics for a Langmuir probe measurement; the probe is movable between the electrodes and the substrate. Optical emission plume illustrating the plasma jet next to the gas flow dependent equipotential lines recorded using the Langmuir probe. (b) Optical emission spectrum of a copper plasma jet at 2000 sccm gas flow rate. (c) Calculated velocity ratio over distance from substrate surface dependent on gas flow rate. (d) Illustration (drawn to scale) depicting the calculated crossover between the carrier gas dominated and electric field dominated transport zone; with increasing gas flow the electric field dominated transport zone becomes thinner.

carrier gas at atmospheric pressure conditions. As the particles come close to the substrate, the transport mechanism is no longer dominated by the carrier gas flow but driven by the emergence of an electric field. This field evolves under steady state condition and a portion of the arriving charged species is collected and neutralized leading to a change in substrate mass. The emissions from the plasma jet, however, indicates that not all the generated material will deposit on it. Some including charged material is spilled in the exhaust. Considering the law of conservation of charge where charge can be created and destroyed only in positive-negative pairs, a loss of charge is not possible; in other words, the spilled charges need to find a path back to the electrical system ground. It is possible to monitor the amount of spilled charges by placing a grounded steel wool plug which acts as a Faraday cup in the exhaust pipe (0,6 m away). The chamber parts are custom-made out of PMMA plastic from Evonik. The ambient works at atmospheric pressure. The incoming nitrogen is dry at 2 bar pre-pressure with a purity of 99.9999% and the flow is controlled by two MKS mass flow controllers with a range of 20–2000 sccm and 200–20000 sccm.

The schematic (Fig. 1b**)** details circuit diagrams and additional elements including a quartz balance and a Langmuir probe. Specifically, carrier gas flow dependent values focusing on (i) the electric potential profile along the trajectory, (ii) the total current leaving the spark region, (iii) the total current collected on the substrate, (iv) the change of mass of the substrate as a result of collected particles, and (v) the spilled charge leaving the reactor through the exhaust.

From an electrical measuring point of view several elements are critical and should be mentioned. First, it was essential to use a 12 V battery-operated spark discharge-based plasma generator to establish a single ground connection to record the total charge leaving the spark region and Faraday cup measurements that led to consistent results. At the same time, the spark current can be recorded. For example, at a coupled power of 3 W the current between the electrodes is 3 mA and a few hundred nA (typically $<0.01\%$) leave the discharge region (generation zone). The spark current was recorded with a Fluke 771 current clamp. The current leaving the discharge region depends on the carrier gas flow rate, in other words the flowing gas sweeps away charged species, it is nearly zero without flow. All currents (excepting the spark current) are recorded with a Fluke 87 RMS Multimeter. To reach the range of pico- and nanoamps, the current is calculated from the measured voltage over the inner resistance of 10 MΩ; 1 V corresponds linear to 100 nA. The polarity of the current leaving the spark region provides a direct measure of the dominating carrier type; the removed particles and charged ions are known to be predominantly positively charged (Fang et al., 2016; Lin et al., 2010) which is confirmed using this measurement. The carrier gas transports (transport zone) this flux of positively charged gas ions and nanoparticles away from the generation zone. The momentum of the gas flow carries the resulting particles and charged gas ions from the source. Due to the inertia, a flow of positive charge carriers is created. This forced electroosmosis generates a measurable transition voltage (Lee, 2007). The flow dependent inertia of the charged particles can in principle be seen as an equivalent voltage source transporting and pushing positively charged particles onto the substrate. Even without applying a bias to the substrate and using only a simple connection to ground a current will flow and can be recorded at the location of the depicted ampere meter (bottom, Faraday cup 2). However, to increase the collection efficiency and reduce the loss of gas ions and charged nanoparticles a negative bias voltage can be applied. To give a number example: A 3 W plasma, a 1 mm electrode gap, and 10000 sccm (standard cubic centimeters per minute) carrier gas, yields two currents, a 165 nA current leaving the discharge region, and 80 nA at the substrate at a modest -500 V additional bias voltage. These values indicate, that approximately 50% of the charged species reach the substrate surface. A quartz balance is capable to measure the mass change on the substrate caused by the collection and continues neutralization of charged species. Both quantities, the electrical dissipation current recorded at the substrate as a result of charge dissipation of gas ions and charged nanoparticles and the change of mass recorded using the quartz balance will be discussed in more detail.

3. Results and discussion

The net ionic particle transport can in principle be described using

$$\overrightarrow{J} = \mathrm{q}\left(- D_n \overrightarrow{\nabla} n + \mu_n \overrightarrow{E} n + \overrightarrow{v_{\mathrm{GF}} n} \right) + \mu_n \overrightarrow{F_g} n \tag{1}$$

where J stands for the ionic current density, q for the electrical charge, D_n for the diffusion constant of charged species, n for the net charged carrier concentration, μ_n for the electric mobility of the charged species, E for the electric field, v_{GF} for the gas velocity, and F_g for the gravity.

In general, the gravitational term is not relevant considering the small (< 10 nm) size of the charged species. Equally, the diffusive fraction resulting from gradients in the particle concentration can be neglected in most areas; it contributes only close to the generation zone and close to the substrate, where the number concentration changes over sufficiently close distances. The generation zone will not be considered in this study. In essence, two regions can be defined: (i) a region sufficiently far away from the substrate where the transport is dominated by the moving carrier gas pointing downwards to the substrate and (ii) a region sufficiently close to the substrate where the transport is dominated by the electric field. As we will show later, the size of the respective regions will depend on the gas flow. Fig. 2a provides the schematic circuit diagram, the optical emission, the electric potential profiles, in Fig. 2b the OES spectrum at 2000 sccm gas flow rate, and in Fig. 2c the drawn to scale crossover between the gas flow dominated transport zone and the electric field dominated transport zone. To establish the crossover between both zones, a Langmuir probe is used to measure the electric potential and calculate field distribution. We are particularly interested to determine the strength of the electric field to compute an electric field-based drift velocity in the various sections. This velocity is compared against the velocity of the carrier gas flow to determine the crossover between the separate regions, i.e. the (i) gas flow and (ii) electric field dominated transport region.

A first indication of the influence of the gas flow can be seen by studying the optical emission plume (photographs, inserts in Fig. 2a)

inside the reactor as a function of the gas flow rate. The plume is recorded with a Nikon D5200 camera combined with a DX VR standard objective in manual mode. Aperture is full opened and recording time is kept at 30 s. The emission is due to an energy loss of excited nanoparticle states (red-orange color). The distribution is not constant. At 200 sccm the emission is limited to the generation zone (not shown). The absence of excited particles in the capture zone indicates that the relaxation time is shorter than the duration of transport. At 2000 sccm excited particles move sufficiently fast to reach the substrate and the optical emission picture resembles the form of the well-established laminar flow profile in a vertical stagnant point reactor. Some spill of excited particles passing the substrate can also be detected. At higher gas flow rates, the region expands, and excited particles appear to be present throughout the reactor. At 14000 sccm we calculated a Reynolds number of 2485, reflecting the 6 mm inlet, a nitrogen density of 1.250 kg/m^3 and a dynamic viscosity of 16.6 μPa s, respectively. A Reynolds number of about 2300 is commonly used to describe the crossover between laminar and turbulent flow. The Supplemental Fig. S1 gives a more comprehensive view on the evolution of the emission picture in the reactor with increasing gas flow rates. In summary, two points can be made. The carrier gas flow rate impacts the particle distribution. Excited nanoparticles reach the substrate at medium (1700 sccm) to high (20000 sccm) flow rates. A well-defined transport layer becomes visible at intermediate (2000–5000 sccm) flows. Some spilling of reactive species is visible, which extend out into the exhaust. The orange glow can be clearly assigned to the copper particles in the spectrum of the plasma in Fig. 2b. Although blue-green shining nitrogen ions and green-yellow shining copper states are also visible in the plasma, the orange color of the copper states appears in the plasma jet itself. The color of the plasma jet depends on the electrode material. The bands around 500 nm are displayed as insert. These show that the peak has very broad shoulders and that there are vibrations, rotations, oscillations as well as reactions with other species. The OES spectrum was recorded with a get.spec spectrometer with a range of 200–1100 nm and a resolution of 0.5 nm.

The Langmuir probe measurements reveal two transport zones; more precisely a gas flow dominated and an E-field dominated zone. In order to gain a deeper insight into the dominant transport mechanism in the various zones, it is important to record the electric field distribution to calculate the anticipate drift velocity of the charge species. The use of a Langmuir probe along the centerline of the setup provides a suitable procedure to get first order estimates. We followed a standard procedure whereby the current of the probe is regulated to zero by means of a counter-voltage. The measurement was performed without a bias on the substrate to investigate potential curves dependent only on gas flow rate. Without a substrate bias it is avoided that an additional capacitive voltage is coupled into the jet, which could change the potential curve. The probe tip is then moved vertically through the reactor and the potential is measured in the center axis along the z-direction. The probe is custom made from a copper wire encapsulated in a ceramic tube. The tip of the probe has a diameter of 30 μm (±5 μm accuracy with caliper) and is encapsulated in a small shrink tube piece. The counter high voltage was regulated and supplied by a Gamma High Voltage block MC50R. Close proximity measurements are using pieces of paper to control the height stepwise. The measured thickness of one piece of paper is 50 μm (±5 μm accuracy with caliper).

The resulting potential profile is not constant. With an increased gas flow (left to right images) the equipotential lines are pushed closer to the substrate. In other words, the gas flow can be seen as an equivalent voltage source. It pushes positive charges downwards leading to an increased potential gradient and electric field above the substrate. We see the increase in electric field as a secondary effect; the electric field increases until a partial balance (neglecting spilled charges) between the electric field and gas flow dominated transport is met.

As an example, we would like to discuss, the results for an intermediate 2000 sccm flowrate and provide some representative numbers for the electric field (the gradient of the depicted potential, grayscale images in Fig. 2a). In general terms the electric field is large in the generation zone (exceeding 400 V/mm) and close to the substrate (exceeding 130 V/mm) and neglectable (smaller 1 V/mm) in the transport zone. To give a number example, the electric field based, drift velocity can be calculated using $v = \mu_n E$ and becomes 0.16 m/s in the center of the transport region where the electric field is 0.75 V/mm. The electric field contributes only a velocity of 0.16 m/s. It is important to estimate at which velocities the system behaves advective rather than diffusive. The Péclet number for mass transfer allows to consider this aspect

$$Pe_l = \frac{L\,v}{D} \tag{2}$$

where L is the characteristic length, v is the velocity and D is the diffusion coefficient of the relevant system. The diffusion coefficient can be calculated using the Einstein-Smoluchowski relation for the mobility of electric charges

$$D = \frac{\mu\ k\ T}{q} \tag{3}$$

where k T /q can be taken together and are assumed to be 25 mV with q = e at room temperature. The calculations are considering an average value for the electrical mobility of $\mu_{N+} = 2.12$ cm^2/V (Saporoschenko, 1965). Regarding the actual velocity maximum of the carrier gas flow in the transport region (0.43 m/s @ 200 sccm, 4.3 m/s @ 2000 sccm, and 43 m/s @ 20000 sccm), the advective term L*v turns out to be more dominant with increasing gas velocity respectively gas flow rate. The gas velocity field has been calculated using CFD in COMSOL (Supplemental **S2**). The distance of 2 cm between the particle generating electrodes and the substrate is the critical length L to calculate the Péclet number. To achieve a Péclet number of 1, which marks the border between advective and diffusive transport, the advective velocity has to reduce to

v = 25 mV * 2.12 cm^2/V / 2 cm = 0.027 cm/s

This velocity correlates with a gas flow rate of approximately 45 sccm.

In other words, a clear conclusion can be drawn. Specifically, we can define and confirm the existence of a transport zone, which is

clearly dominated by the gas velocity instead of the electric field. Within the gas flow dominated transport region equation (1) reduces to:

$$\vec{J} = q\overrightarrow{v_{GF}}n \tag{4}$$

A second conclusion can be drawn. It turns out that the gas flow is the driver, not only for the particle velocity in this zone but also for the distribution of the potential and electric field in most regions of the reactor. To understand this second statement, let us further consider the grayscale images of the equipotential lines (Fig. 2a), in particular the 100 V value to provide a suitable guidance for the eye. With an increasingly high gas flow the 100 V potential is pushed downstream to the surface of the substrate. In other words, the electric field is not simply constant, but predominantly a function of the gas flow rate. At this point we would like to mention that no bias voltage is necessary to get a dissipation current at the substrate. Fig. S1 provides the dependency of the collected charged particles

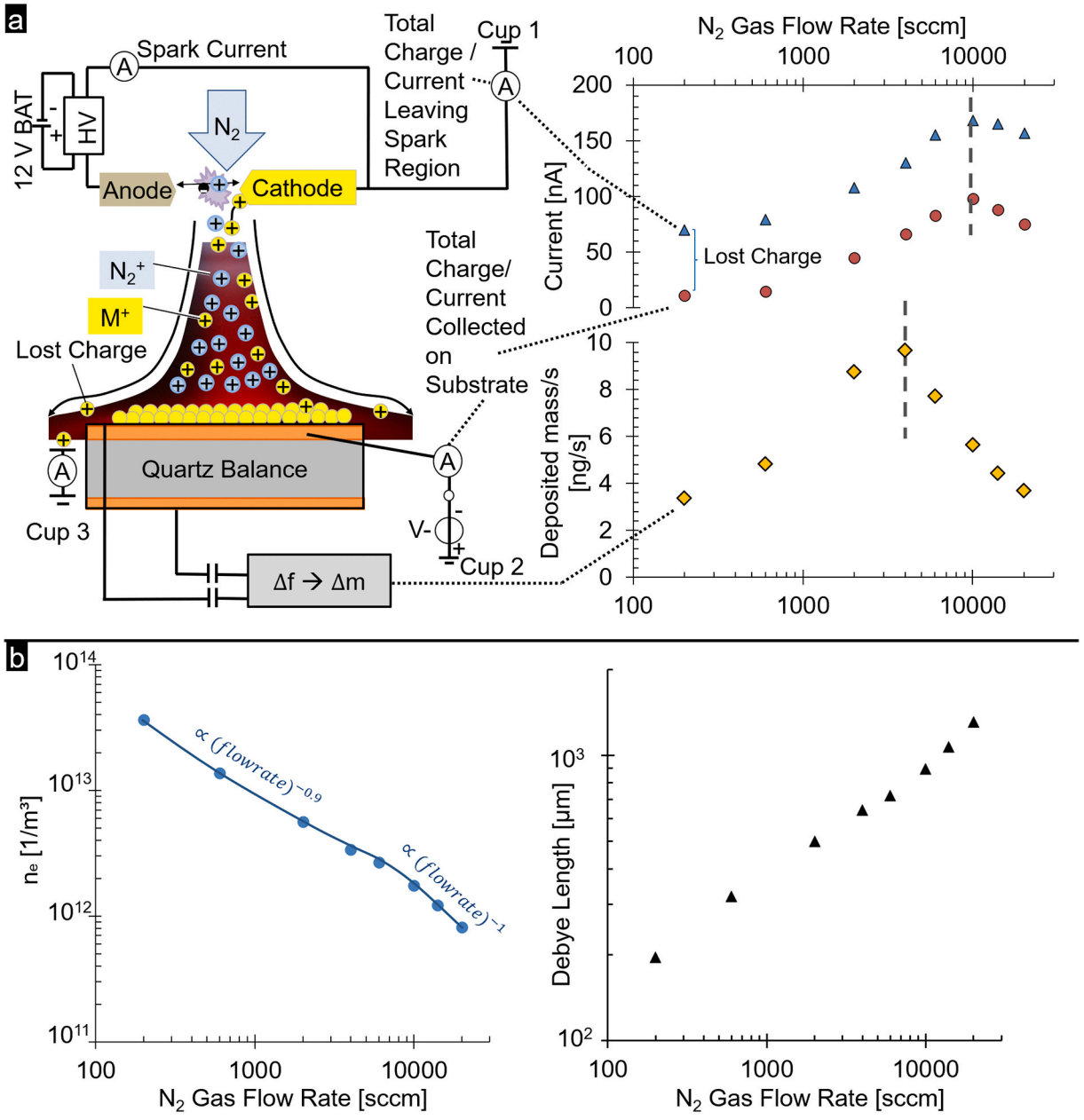

Fig. 3. Schematic and results of the current and mass measurement.(a) The schematic details circuit diagrams, locations of Faraday cups (cups 1–3) and a quartz balance to record carrier gas flow dependent values; specifically, the (i) current leaving the spark region (cup 1), (ii) current collected on the substrate (cup 2), (iii) spilled current into the exhaust (cup 3), (iv) deposited mass on the substrate as a result of collected particles. (b) The left curve evaluates the gas flow dependent charge carrier concentration to calculate the corresponding Debye length (right curve).

(nanoparticles and gas ions) recorded as a dissipation current as a function of the bias voltage; the charged particles will be collected at the substrate even at 0 V bias. In other words, the gas flow pushes the charged particles onto the surface even for a substrate, which is held at ground potential, a current is recorded.

Following equation (2), the gas flow is driving the current in the first place, in effect it is pushing charged species onto the substrate surface. Close to the substrate an electrical field gradient will emerge. The transport will change from a gas flow driven to a field driven condition with an electric field component that points to the surface; however, this can be seen as a secondary effect. The thickness of this electric field dominated transport layer is not constant but a function of the gas flow. If more charges are pushed onto the substrate, a higher electric field gradient is established to accommodate the higher current condition. Within the electric field dominated transport region equation (1) reduces to

$$\overrightarrow{J} = \mathrm{q}\mu_n \overrightarrow{E} n. \tag{5}$$

The ratio of both velocities is calculated by

$$\text{velocity ratio} = \frac{\overrightarrow{v_{\mathrm{GF}}}}{\mu_n \overrightarrow{E}}. \tag{6}$$

Fig. 2c shows three ratio plots over the distance from the substrate surface. The ratio increases as the gas flow increases. As discussed before, both proportions are dependent on the gas flow since it is affecting the electric field distribution as well. Even at 200 sccm gas flow rate the gas velocity is the driver of the transport. Equations (4) and (5) can be set equal to define a crossover between both regions. The crossover in z-direction above the substrate occurs were the gas velocity is equal to the electric field driven drift velocity $\overrightarrow{v_{\mathrm{GF}}} = \mu_n \overrightarrow{E}$. The z-values for a ratio of one are illustrated in Fig. 2d. For gas flow rates smaller than 200 sccm the thickness of the electric field dominated transport layer is larger than 2.5 mm. With increasing gas flow (2000 sccm) the electric field dominated transport zone becomes smaller than 500 μm. Finally, at high gas flow rates larger than 20000 sccm the electric field dominated transport zone becomes thinner than 250 μm.

The growth characteristics on the substrate will be considered later in an experiment. First the current in the transport zone is examined in more detail. Fig. 3 provides the schematics to record all currents and the deposited mass to evaluate the charge carrier concentration to calculate the Debye screening length in the gas flow dominated transport region.

Current measurements in Fig. 3a reveal the ratios between generated, captured, and spilled charges. To further validate these points, we aimed to record ionic current flows using electrometers as depicted in the schematics (Fig. 3a, left). Any charge that leaves the spark region is drawn from the ground connection, and monitoring is possible using the depicted electrometer. A second electrometer is attached between the substrate and the system ground. The second electrometer records the total charge collected and dissipated by the substrate. A third electrometer is used to record the spilled charges. The third electrometer is placed between the system ground and a steel wool plug in the exhaust line (0.6 m away). The sum of the three currents should be near to zero; this was validated; the recorded sum was $< 5\%$ of the current that leaves the spark region which confirms that no unaccounted leakage currents exist in the system. The curves to the right plot the results. The upper curve (blue triangles) describes the current leaving the generation zone, the middle depicts (red circles) the resulting substrate current. The difference is the current which is spilled into the exhaust (bracket between both curves). All currents follow the same general behavior. Starting from 1 sccm with almost no current leaving the spark region the swept away current begins to increase. The value increases up to a flow rate of 10000 sccm where it approaches a maximum of 160 nA. The increased gas flow thus sweeps away more charges out of the generation zone through the transport zone to the substrate and more particles reach the surface. After reaching the maximum of 10000 sccm all currents decrease. It is not clear as to why fewer charges are swept away at this point. As mentioned, some particles are spilled into the exhaust. A relative collection efficiency I_{sub}/I_{top} can be defined. The collection efficiency improves steadily from an initial value of 15% (at 200 sccm) to about a 50% (at 10000 sccm); the 50% value is maintained until the end of the measurement series (20000 sccm).

The recorded current in the generation zone (total charge current leaving the spark discharge) represents the net rate of positively charged nanoparticles and gas ions which leave the generation zone. The recorded current (plot blue triangles) shows that the gas flow has an effect. With an increased gas flow more charges are swept away from the spark region. However, the increase is not linear and there is a clear maximum. The maximum is again at about 10000 sccm, however this maximum current does not correlate with the highest deposition rate (discussed later). Interestingly, the recorded change is not linear. Moreover, it is not a strong dependency, for example, a 100-fold increase in the gas flow rate (from 200 sccm to 20000 sccm) increases the current only by a factor of 2.

The gas flow has a large effect on the volume number concentration and the Debye screening length. With an increase in the carrier gas flow a high level of dilution is a result. First, a calculation of the net volume number charge concentration n is possible using equation (2). The concentration can be written in the form of

$$n = \frac{\mathrm{J}}{\mathrm{q}v_{GF}} = \frac{\mathrm{J}\cdot\mathrm{A}}{\mathrm{q}\cdot v_{GF}\cdot A} = \frac{I}{q\cdot \mathrm{Gasflowrate}} \tag{7}$$

Fig. 3b depicts a volume number charge concentration, which is roughly proportional to the inverse gas flow rate as described by equation (6). Moreover, the obtained charge concentration can also be used to calculate the Debye screening length λ_d, using

$$\lambda_d = \sqrt{\frac{\varepsilon k_B T_e}{n_e e^2}} \tag{8}$$

where ε_0 stands for the dielectric constant, e for the elementary charge, and k_B for the Boltzmann constant. The temperature $T_e = 300$ K is assumed to be a constant in the transport zone far from spark discharge and far from the accumulating substrate (capture zone). The Debye length increases with increasing gas flow. Thus, the effective length of the electrical potential of the charged species increases with the gas flow. As already mentioned in the introduction, experiments in the fabrication of nanostructures have shown that the structures become smoother with increasing gas flow (Fang et al., 2016). We believe that the charge concentration including the effective screening length is critically important. The increased gas flow dilutes the number of charged species per volume in the transport zone. This means that on one hand the same number of charged species reach the surface per second, but on the other hand the increased gas flow rate transports the species at a larger distance from each other and the effective length of the electrical potential of the species increases as well. This might be the reason as to why a more organized capture and deposition process is observed. As an example, the screening length is 200 μm at 200 sccm and 1 mm at 14000 sccm in the transport zone.

The collected mass measurements reveal a gas flow dependent ratio between charged gas ions and charged nanoparticles. Both gas ions and charged nanoparticles are present in the reactor. Both species contribute to the recorded currents. To determine the ratio of the charged species, which arrive at the substrate, we modified a quartz crystal balance to record the mass change of the substrate. The location of the quartz crystal is depicted in the schematic **(**Fig. 3a, left**)**. The change in mass is only due to an accumulation of metallic nanoparticles; the gas ions become neutralized and contribute to the recorded current but remain volatile and do not contribute to the change in mass. The calculation of the particle flux in particles per second requires the average particle size; Transmission electron microscopy (TEM) was used to determine the reported values; the supplemental section **S3** provides more details about the TEM measurements. In any event a deposition rate in particles per time (e.g.: 10^9 /s at 600 sccm) can be determined and this value can be compared to the total substrate current in elementary charges per second (e.g.: 8×10^{11} elementary charges per second at 600 sccm).

However, to correctly monitor the mass deposition rate, a quartz crystal is required. A quartz crystal (Inficon) with 1 cm in diameter with a circular metallic electrode to dissipate the flux of incoming charges was used in the experiments. The electrode is important; gas-phase electrodeposition needs an electrode (shown in orange and as a photograph in supplemental section **S4**) to enable charge dissipation. A crystal without electrode records no change in mass since all the charged nanoparticles are spilled into the exhaust. With electrode, the quartz crystal balance equation

$$\Delta m = m_0 \left(\frac{f_0^2}{f_1^2} - 1 \right) \tag{9}$$

can be applied where Δm is the change in mass as a result of nanoparticle deposition, where f_0 represents the start frequency of the measurement, f_1 the end frequency after a certain time of measurement, and m_0 the pre-measured mass of the quartz chip. The Sauerbrey equation was not applied in these experiments. It only provides good results for the special case of thin and rigid layers and is especially adapted to evaporation experiments (Sauerbrey, 1959; Steinem & Janshoff, 2007). A more detailed theory is given by the transmission line model, which is neglected as well. Since the quartz was able to oscillate freely in air, as mentioned above, we have neglected the mechanical constraints of clamping. A simple mechanical approach of the oscillation equation is chosen. In this approach, the mass of the quartz chip before the experiments serves as a fixed point for calculating all further changes. The mass of the chip was measured before the experiments by a microbalance with $\pm$ 10 mg. The frequencies were measured with an accuracy of 1 Hz. The measurement accuracy of the change in mass thus results from the high accuracy of the frequency measurement. The quartz balance is custom-made out of Inficon chips, which are soldered to a strong copper wire on top and a flexible copper wire on the bottom. The stronger copper wire on the top is the mechanical fix point. The chip was triggered by an oscillator STM2 USB thickness rate monitor from Inficon and an SQM-160 monitor from Sigma Instruments. The frequency mode is used to get the raw data for mass calculation.

Starting at 200 sccm, the mass deposition rate (yellow curve, Fig. 3a) increases until it reaches a maximum at about 4000 sccm before it begins to drop. The onset of the drop is earlier when compared to the total current collected by the substrate. The exact reason is not known. A first explanation could be the higher electrical mobility of the gas ions when compared to the charged nanoparticles. In other words, at higher gas flows the charged nanoparticles do not reach the substrate surface due to an insufficient electrical mobility when compared to the smaller gas ions. The onset and spill of nanoparticles should occur at an earlier state. However, it may also be the case, that the generation rate of nanoparticles decreases at higher gas flow rates; we witness a change in the shape of the spark (elongation) at high flowrates and took comparative weight measurements of the cathode after 100 h of erosion; the erosion drops under high flow conditions, which supports the second hypothesis of a decreased nanoparticle generation rate. Afterwards we measured the mass difference of the electrodes and the substrate with a mircobalance. It turned out, that for example the electrodes at 4000 sccm gas flow rate lost 6 mg, while the substrate mass increased by 4 mg. The number on the substrate correlates with the in-situ quartz balance measurements. This means, that 66% of the particles get collected on the substrate.

At the substrate a current is recorded. This current is produced through charge dissipation of volatile gas ions and non-volatile nanoparticles. An estimate for the ratio between the total number of charged particles and charged nanoparticles can be given. As an example, at 4000 sccm about 48 gas ions arrive at the substrate for every nanoparticle which is deposited. However, the ratio is not constant, at high flow rates charged nanoparticles spill into the exhaust. A Debye length of 200 μm was calculated for a gas flow rate of 200 sccm. The length is strongly dependent on and increases with increasing gas flow rate. A Debye length of 1.3 mm was calculated for a gas flow rate of 20000 sccm.

The previous paragraph estimated a ratio between a charged gas ion flux and charged nanoparticles flux, which arrives at the substrate surface. The values were determined using the current and mass measurements at the substrate. The previous discussion used simplified equations, where the number concentration n was used as a cumulative value of both charged nanoparticles and gas ions.

The equations provided a good first order estimate since the number concentration of charge nanoparticles is at least one order of magnitude smaller than the number concentration of charged gas ions. However, the equations can be expanded to provide a more exact value. For example, the net current on the substrate can be written as

$$I = q\left(\dot{N}_{N2} + \dot{N}_p\right) = q\left(\dot{V}\left(n_{N2} + n_p\right) + A\,E\left(\mu_{N2} n_{N2} + \mu_p n_p\right)\right) \tag{10}$$

where q stands for the charge per species, $\dot{N}_{N2}$ for the flux of nitrogen ions per second, $\dot{N}_p$ for the flux of charged metal particles per second, $\dot{V}$ for the gas flow rate, A for the cross-section area, n_{N2} for the volume number nitrogen ion concentration, n_p for the volume number charged nanoparticle concentration, μ_{N2} for the mobility of the gas ions, and μ_p for the mobility of the charged nanoparticles. As in the previous discussion, $\dot{N}_p$ the flux of charge metal particles per second, can be measured indirectly at the substrate surface in terms of a mass deposition rate $\dot{m}$; specifically, $\dot{N}_p = \dot{m}/m_{particle}$. Equally, the recorded dissipation current provides a value for $\dot{N}_{N2} + \dot{N}_p = \frac{I}{q}$. This results in the following equation, which allows us to calculate the number of nitrogen ions $\dot{N}_{N2}$ using the following equation

$$\dot{N}_{N2} = \dot{N}_e - \dot{N}_p = \frac{I}{q} - \frac{\dot{m}}{m_{particle}} \tag{11}$$

The nanoparticles were found to be round (STEM images in supplemental **S3**) and a mass per particle was calculated. The particle

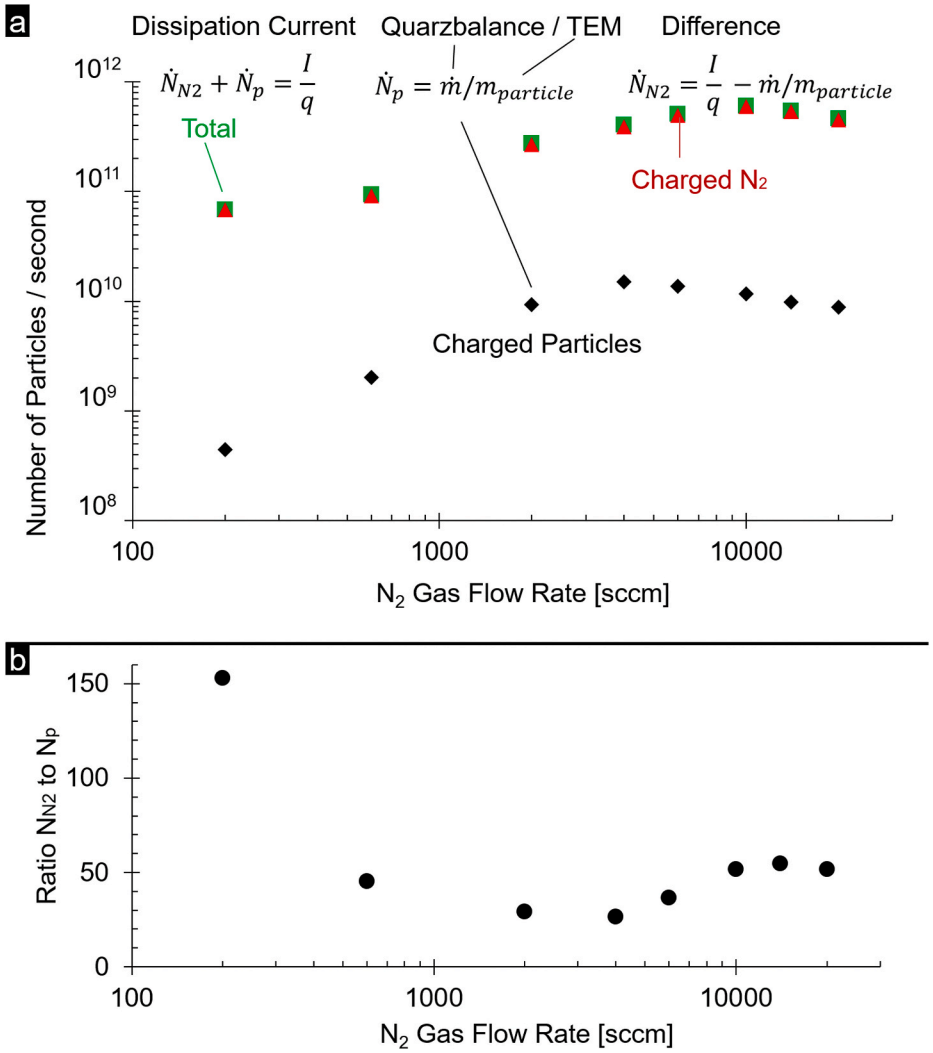

Fig. 4. (a) Recorded flux of charged species as a function of the gas flow; total charged species (green squares) composed of Nitrogen ions (red triangles) and charged nanoparticles (black diamonds); (b) ratio between nitrogen ions and charged metal particles. (For interpretation of the references to color in this figure legend, the reader is referred to the Web version of this article.)

size is flow dependent; Fig. S3. For example, at 2000 sccm the average particle diameter is 5 nm and the particle mass is 1.26×10^{-18} g, using 19.32 g/cm^3 (gold) as the density. A 5 nm sized particle is sufficiently small to limit the amount of charges (space charge limitation) to predominantly a single elementary charge (Lowe & Lucas, 1953; White, 1951). In case of the gas ions it is also assumed that every ionized molecule carries a single elementary charge, which means that q = e.

Fig. 4a depicts the gas flow dependency of the total ionic current collected on the substrate. Values for the charged nitrogen ions $\dot{N}_{N2}$ and charged metal particles $\dot{N}_p$ in particles per second are given. The results confirm that nitrogen ions are responsible for a large portion of the dissipation current; again, the flux of Nitrogen ions exceeds the nanoparticle flux by approximately two orders of magnitude (Fig. 4b). The maximum collection rate of charged metal particles is reached at 4000 sccm, which corresponds to the minimum in the ratio between gas ions and charged metal particles. This is interesting since it points to a sorting process. Going back to the generation zone (Fig. 3a), we found 10000 sccm to be the condition where the maximum amount of charges is swept away from the discharge region. However, the flow rate of 10000 sccm appears to be too high for nanoparticles. In other words, a sorting process is present. In the deposition zone the electric field vector points downwards. However, the vector of the gas velocity points to the outside of the substrate holder. Nanoparticles have the lowest electrical mobility and will be spilled first and gas ions spill last. The two shoulders (at 4000 sccm and at 10000 sccm) in the curves are therefore interesting. The drop at 4000 sccm due to a spill of metal particles (yellow diamond curve) and 10000 sccm due to a spill of gas ions (red circle curve).

The particle properties in combination with the different deposition rate regimes have an influence on the film morphology when thin films are deposited on the substrate at different gas flow rates and spark discharge power. Based on the high dilution of the metal particles in nitrogen gas and a very small mean free path at atmospheric pressure, Thornton's structure zone model (Thornton, 1977) is not valid here. Fig. 5 reveals that the film morphology and deposition rate is a function of the gas flow rate and spark power. The deposition time (5 min) is kept constant. The series test the formation of nickel films. Very similar relationships have been found for other metals. Low spark power combined with low gas flow leads to dendritic films (red box). At intermediate spark power and gas flow rates the dendritic nature remains; however, an increased compactness and film thickness can be noticed (yellow box). At higher spark power and gas flow rates the compactness increases further (green box) and a reduction in film thickness is observed.

From the left to the right columns we notice an eventual drop in film thickness. This drop is independent of the power level. It typically occurs exceeding 2000 sccm (center column). This drop can be directly associated with the spill of particle into the exhaust. However, the films also appear to become more compact. The increased compactness may be associated to a reduced particle size. Images of the primary particle size are in the supplemental section S3. As an example, at 100 sccm and 2.5 W the particle size is 5 nm. The size reduces to 2 nm at 10000 sccm and 2.5 W. A second and previously not considered concept has to do with the dilution levels, specifically the volume number concentration (n_e). As the gas flow increases, the volume number concentration drops which may

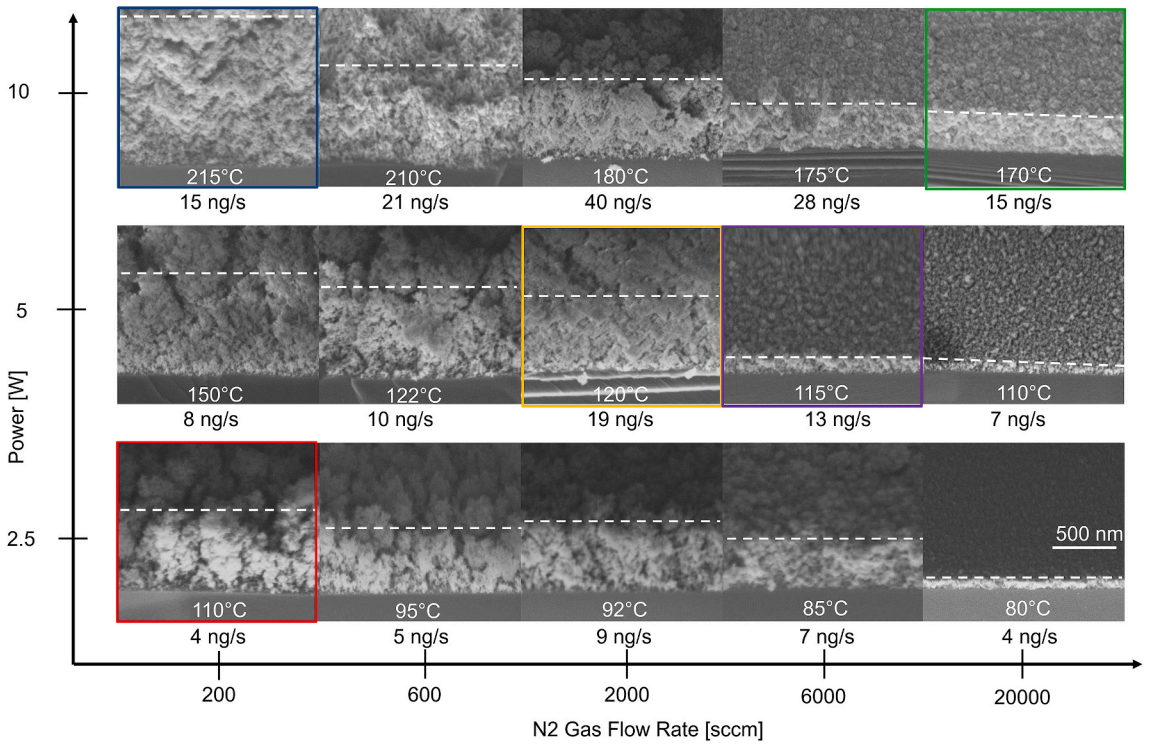

Fig. 5. Film morphology (SEMs), values of the mass deposition rate (Δm) and affected substrate temperature as a function of various flow rates (logarithmic scale) and spark powers (linear scale). The white dashed line aims to aid the eye to show the edge of the film. The micrographs were recorded under an angle of 45° to show both the cross section and the top morphology.

prevent aggregation in the transport zone. As a result, the structures can grow more orderly. A third parameter may have to do with the kinetic energy of a particle hitting the surface. The temperature as a result of that impact is measured on top of the substrate surface using a thermo couple. As the gas flow increases, the substrate temperature is affected by the cooling mechanism of the gas flow. This indicates that the particle kinetics are not the driver for the increasing compactness. From the bottom to the top row we notice a rise in the film thickness and mass deposition rate. The mass deposition rate scales nearly linear with the spark power. This is not the case for the film thickness. This can be understood since the film morphology is influenced. Dendritic films (e.g. blue colored box) are less compact and therefore thicker when compared to less dendritic films (e.g. violet and green colored box) with the same mass deposition rate. The diffusion contributes with a velocity of 0.27 mm/s. Below 600 sccm this proportion has an impact, which also explains the dendritic growth. The sorting mechanism, which results from the interaction between gas flow and electric field, is driven upwards by the increase in gas flow. There is also a general tendency that a higher power level leads to more compact layers. This is counter intuitive since the primary particle size and size distribution will increase with the spark power (Barankin, Creyghton, & Schmidt-Ott, 2006; E. Garwin & Schwyn, 1988; Feng, Guo, et al., 2016b; Tabrizi et al., 2009). There might be a second parameter that is influencing the order. The substrate temperature depicts that more power in the generation zone leads to an increasing temperature transfer to the substrate. As an example, at 200 sccm and 2.5 W the substrate temperature is 110 °C. The temperature increases to 215 °C at 200 sccm and 10 W. Though, the incoming larger particles transport more kinetic energy, move longer on the surface, fill cavities and produce denser structures.

Fig. 6 enables a closer look to four characteristic samples from the previous figure. The images show cross-sectional views of the outer four corners of the maximum parameter range of analyzed spark power and gas flow rate. The images were taken under 4° angle

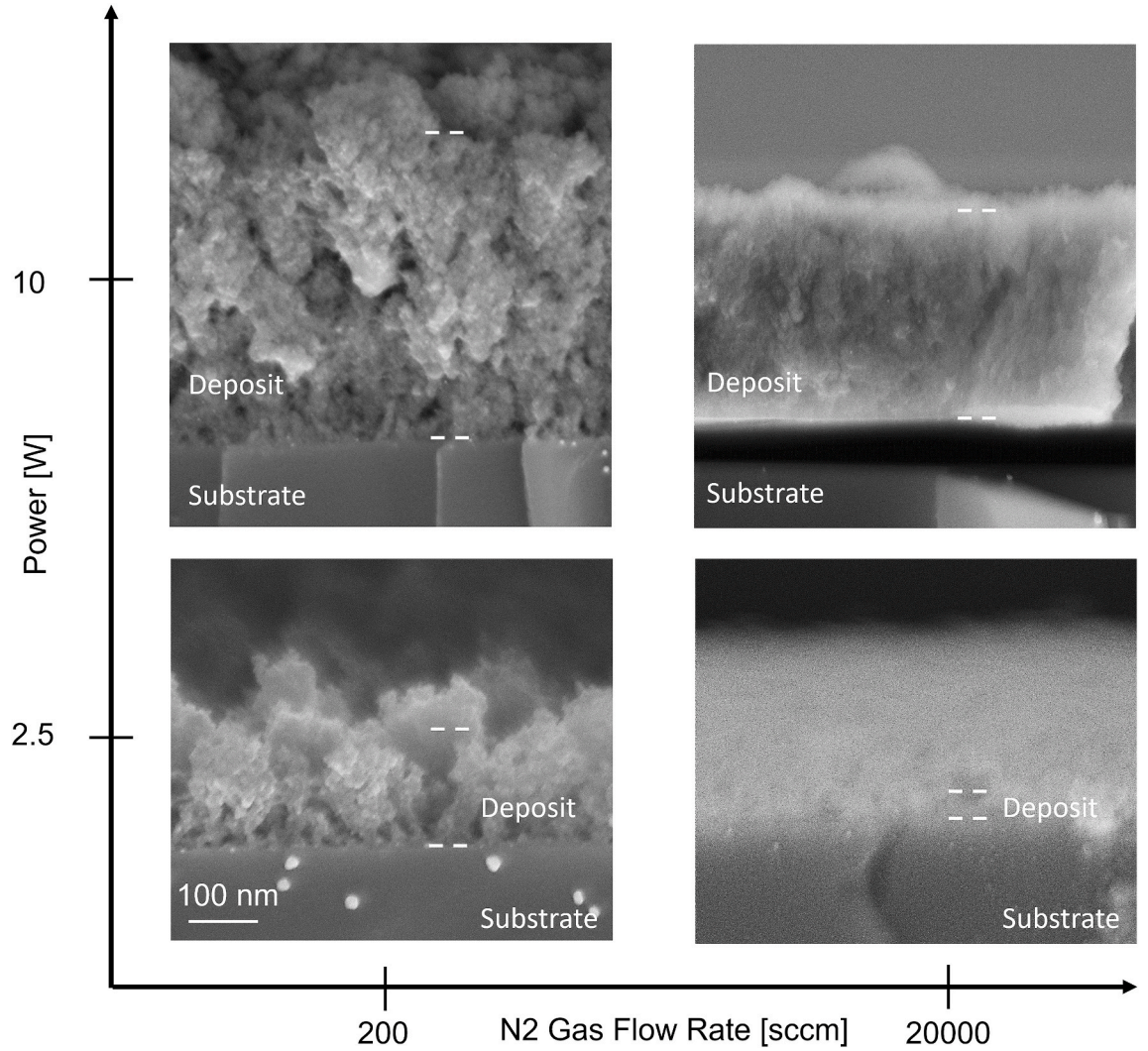

Fig. 6. High-resolution cross-sectional film morphology (SEMs) at various flow rates (logarithmic scale) and spark powers (linear scale). The white dashed line aims to aid the eye to show the edge of the film. The micrographs were recorded under an angle of 4° to show next to the cross section a slight imagination of the top morphology.

to get a slight imagination of the film top morphology. The cross-sectional views underline the statements from Fig. 5, that low gas flow rate and low spark power lead to dendritic structures. On the other hand, high gas flow rate and high spark power increase the compactness. While the image at 20000 sccm and 2.5 W shows still cavities, the 4-fold increased spark power uncovers at the same gas flow rate a compact layer. This layer acts as a solid body and starts to delaminate, which can be seen in the dark shadow between the substrate and the layer. Even the obliquely broken facet of the substrate is formed in the layer, which indicates high mechanical strength. Considering the deposition kinetics, it concludes that the determined maximum of the metal particle rate, which also correlates with the minimum ratio to the gas ions, and the maximum of the outflowing current represent two transition points. Below the maximum deposition rate, structures grow predominantly dendritically, indicating column growth. Between 4000 sccm and 10000 sccm there is a transition area that allows the formation of irregular porous layers. Above 10000 sccm the structures show layer growth properties. Looking at the expected structures from previous particle growth simulations or from inertial impaction experiments, the layers shown here appear to have a surprisingly good packing density at a gas flow of 20000 sccm and a power of 10 W. The key is probably the low growth rate. This rate results from the transition from a carrier gas dominated into an electric field dominated transport zone in a very thin volume above the substrate. Thus, only the fastest particles are trapped. These highly diluted fast particles allow a layer growth characteristic.

4. Conclusion

The Langmuir Probe measurements reveal two transport zones - a gas flow dominated and an E-field dominated zone. It turns out that the gas flow is the driver, not only for the particle velocity in the transport zone but also for the distribution of the potential and electric field in most regions of the reactor. Close to the substrate an electrical field gradient will emerge. The transport will change from a gas flow driven to an E-field driven condition with an electric field component that points to the surface. The Debye length in the transport zone is directly dependent on the gas flow rate. The electric current and deposited mass measurements indicate that nitrogen ions are in the clear majority compared to the metal particles from the spark discharge. An estimate for the ratio between the total number of charged particles and charged nanoparticles can be given. As an example, at 4000 sccm about 48 gas ions arrive at the substrate for every nanoparticle which is deposited. However, the ratio is not constant, at high flow rates charged nanoparticles spill into the exhaust. A Debye length of 200 μm was calculated for a gas flow rate of 200 sccm. The length is strongly dependent on and increases with increasing gas flow rate. A Debye length of 1.3 mm was calculated for a gas flow rate of 20000 sccm, which indicates that with every magnitude of increasing gas flow rate the Debye length is increasing half a magnitude. The parameters gas flow rate and spark discharge power affect measurable quantities such as the electrical current carried by the charged nanoparticles and gas ions, the nanoparticle mass, particle size and film morphology. Considering the film morphology, the power of the discharge turns out to be the most relevant parameter. Low spark power combined with low gas flow leads to dendritic film growth. In contrast, higher spark power combined with higher gas flow produces compact layers. This two-dimensional parameter field enables a tailored film morphology and deposition rate. The methods applied complement the previous applications.

Declaration of competing interest

The authors declare that they have no known competing financial interests or personal relationships that could have appeared to influence the work reported in this paper.

Acknowledgements

The research is funded in parts by grant from the German Science foundation DFG JA1023/4-1, STA 556/4-1, and by a grant from the foundation for electrostatics ELSTATIK.

Appendix A. Supplementary data

Supplementary data to this article can be found online at https://doi.org/10.1016/j.jaerosci.2020.105652.

References

Bae, Y., Pikhitsa, P. V., Cho, H., & Choi, M. (2017). Multifurcation assembly of charged aerosols and its application to 3D structured gas sensors. *Advanced Materials, 29*(2). https://doi.org/10.1002/adma.201604159.

Barankin, M. D., Creyghton, Y., & Schmidt-Ott, A. (2006). Synthesis of nanoparticles in an atmospheric pressure glow discharge. *Journal of Nanoparticle Research, 8*, 511–517. https://doi.org/10.1007/s11051-005-9013-1.

Barry, C. R., & Jacobs, H. O. (2006). Fringing field directed assembly of nanomaterials. *Nano Letters, 6*(12), 2790–2796. https://doi.org/10.1021/nl0618703.

Barry, C. R., Steward, M. G., Lwin, N. Z., & Jacobs, H. O. (2003). Printing nanoparticles from the liquid and gas phases using nanoxerography. *Nanotechnology, 14*(10), 1057–1063. https://doi.org/10.1088/0957-4484/14/10/301.

Binions, R., & Naik, A. J. T. (2013). Metal oxide semiconductor gas sensors in environmental monitoring. In *Semiconductor gas sensors*. https://doi.org/10.1533/9780857098665.4.433.

Bitterle, E., Karg, E., Schroeppel, A., Kreyling, W. G., Tippe, A., Ferron, G. A., et al. (2006). Dose-controlled exposure of A549 epithelial cells at the air-liquid interface to airborne ultrafine carbonaceous particles. *Chemosphere*. https://doi.org/10.1016/j.chemosphere.2006.04.035.

Brewer, D. D., Shibuta, T., Francis, L., Kumar, S., & Tsapatsis, M. (2011). Coating process regimes in particulate film production by forced-convection-assisted drag-out. *Langmuir*. https://doi.org/10.1021/la202040x.

Byeon, J. H., Park, J. H., & Hwang, J. (2008). Spark generation of monometallic and bimetallic aerosol nanoparticles. *Journal of Aerosol Science, 39*(10), 888–896. https://doi.org/10.1016/j.jaerosci.2008.05.006.

Castillo, J. L., Martin, S., Rodriguez-Perez, D., Higuera, F. J., & Garcia-Ybarra, P. L. (2018). Nanostructured porous coatings via electrospray atomization and deposition of nanoparticle suspensions. *Journal of Aerosol Science*. https://doi.org/10.1016/j.jaerosci.2018.03.004.

Cole, J. J., Lin, E. C., Barry, C. R., & Jacobs, H. O. (2009). Continuous nanoparticle generation and assembly by atmospheric pressure arc discharge. *Applied Physics Letters, 95*(11). https://doi.org/10.1063/1.3197646.

Cole, J. J., Lin, E. C., Barry, C. R., & Jacobs, H. O. (2010). Mimicking electrodeposition in the gas phase: A programmable concept for selected-area fabrication of multimaterial nanostructures. *Small, 6*(10), 1117–1124. https://doi.org/10.1002/smll.200901547.

Cole, J. J., Wang, X., Knuesel, R. J., & Jacobs, H. O. (2008). Integration of ZnO microcrystals with tailored dimensions forming light emitting diodes and UV photovoltaic cells. *Nano Letters*. https://doi.org/10.1021/nl0804809.

Fang, J., Park, S. C., Schlag, L., Stauden, T., Pezoldt, J., & Jacobs, H. O. (2014a). Active matrix-based collection of airborne analytes: An analyte recording chip providing exposure history and finger print. *Advanced Materials, 26*(45), 7600–7607. https://doi.org/10.1002/adma.201402589.

Fang, J., Park, S. C., Schlag, L., Stauden, T., Pezoldt, J., & Jacobs, H. O. (2014b). Localized collection of airborne analytes: A transport driven approach to improve the response time of existing gas sensor designs. *Advanced Functional Materials, 24*(24), 3706–3714. https://doi.org/10.1002/adfm.201303829.

Fang, J., Schlag, L., Park, S. C., Stauden, T., Pezoldt, J., Schaaf, P., et al. (2016). Approaching gas phase electrodeposition: Process and optimization to enable the self-aligned growth of 3D nanobridge-based interconnects. *Advanced Materials, 28*(9), 1770–1779. https://doi.org/10.1002/adma.201503039.

Feng, J. (2017). *Scalable spark ablation synthesis of nanoparticles: Fundamental considerations and application in textile nanofinishing*. TU Delft University. https://doi.org/10.4233/uuid.

Feng, J., Guo, X., Ramlawi, N., Pfeiffer, T. V., Geutjens, R., Basak, S., et al. (2016a). Green manufacturing of metallic nanoparticles: A facile and universal approach to scaling up. *Journal of Materials Chemistry A*. https://doi.org/10.1039/c6ta03221d.

Feng, J., Hontañón, E., Blanes, M., Meyer, J., Guo, X., Santos, L., et al. (2016b). Scalable and environmentally benign process for smart textile nanofinishing. *ACS Applied Materials and Interfaces, 8*(23), 14756–14765. https://doi.org/10.1021/acsami.6b03632.

Feng, J., Ramlawi, N., Biskos, G., & Schmidt-Ott, A. (2018). Internally mixed nanoparticles from oscillatory spark ablation between electrodes of different materials. *Aerosol Science and Technology*. https://doi.org/10.1080/02786826.2018.1427852.

Garwin, E., & Schwyn, S. (1988). *Aerosol generation by spark discharge, 19*(5), 639–642. A. S.-O.

Ha, K., Choi, H., Jung, K., Han, K., Lee, J. K., Ahn, K., et al. (2014). Large-area assembly of three-dimensional nanoparticle structures via ion assisted aerosol lithography with a multi-pin spark discharge generator. *Nanotechnology*. https://doi.org/10.1088/0957-4484/25/22/225302.

Higuera, F. J. (2018). Structure of deposits formed from electrosprayed aggregates of nanoparticles. *Journal of Aerosol Science*. https://doi.org/10.1016/j.jaerosci.2018.01.007.

Hou, Y., Kondoh, H., Ohta, T., & Gao, S. (2005). Size-controlled synthesis of nickel nanoparticles. *Applied Surface Science, 241*(1–2), 218–222. https://doi.org/10.1016/j.apsusc.2004.09.045.

Isaac, N. A., Valenti, M., Schmidt-Ott, A., & Biskos, G. (2016). Characterization of tungsten oxide thin films produced by spark ablation for NO2 gas sensing. *ACS Applied Materials & Interfaces, 8*(6), 3933–3939. https://doi.org/10.1021/acsami.5b11078.

Jacobs, H. O. (2001). Submicrometer patterning of charge in thin-film electrets. *Science, 291*(5509), 1763–1766. https://doi.org/10.1126/science.1057061.

Jacobs, H. O., Campbell, S. A., & Steward, M. G. (2002). Approaching nanoxerography: The use of electrostatic forces to position nanoparticles with 100 nm scale resolution. *Advanced Materials, 14*(21), 1553–1557. https://doi.org/10.1002/1521-4095(20021104)14:21<1553::AID-ADMA1553>3.0.CO;2-9.

Jung, K., Hahn, J., In, S., Bae, Y., Lee, H., Pikhitsa, P. V., et al. (2014). Hotspot-engineered 3D multipetal flower assemblies for surface-enhanced Raman spectroscopy. *Advanced Materials*. https://doi.org/10.1002/adma.201401004.

Kuznetsov, B. V., Rakhmanova, T. A., Popovicheva, O. B., & Shonija, N. K. (2003). Water adsorption and energetic properties of spark discharge soot: Specific features of hydrophilicity. *Journal of Aerosol Science, 34*(10), 1465–1479. https://doi.org/10.1016/S0021-8502(03)00366-5.

Lee, Y. S. (2007). Self-Assembly and nanotechnology: A force balance approach. Self-assembly and nanotechnology: A force balance approach. https://doi.org/10.1002/9780470292525.

Lin, E. C., Cole, J. J., & Jacobs, H. O. (2010). Gas phase electrodeposition: A programmable multimaterial deposition method for combinatorial nanostructured device discovery. *Nano Letters, 10*(11), 4494–4500. https://doi.org/10.1021/nl102344r.

Lindquist, G. J., Pui, D. Y. H., & Hogan, C. J. (2014). Porous particulate film deposition in the transition regime. *Journal of Aerosol Science*. https://doi.org/10.1016/j.jaerosci.2014.03.007.

Lin, E. C., Fang, J., Park, S. C., Johnson, F. W., & Jacobs, H. O. (2013a). Effective localized collection and identification of airborne species through electrodynamic precipitation and SERS-based detection. *Nature Communications, 4*. https://doi.org/10.1038/ncomms2590.

Lin, E. C., Fang, J., Park, S. C., Stauden, T., Pezoldt, J., & Jacobs, H. O. (2013b). Effective collection and detection of airborne species using SERS-based detection and localized electrodynamic precipitation. *Advanced Materials, 25*(26), 3554–3559. https://doi.org/10.1002/adma.201300472.

Lowe, H. J., & Lucas, D. H. (1953). The physics of electrostatic precipitation. *British Journal of Applied Physics, 4*(S2). https://doi.org/10.1088/0508-3443/4/S2/317.

Mädler, L., Lall, A. A., & Friedlander, S. K. (2006). One-step aerosol synthesis of nanoparticle agglomerate films: Simulation of film porosity and thickness. *Nanotechnology*. https://doi.org/10.1088/0957-4484/17/19/001.

Messing, M. E., Dick, K. A., Wallenberg, L. R., & Deppert, K. (2009). Generation of size-selected gold nanoparticles by spark discharge — for growth of epitaxial nanowires. *Gold Bulletin, 42*, 20–26. https://doi.org/10.1007/BF03214902.

Messing, M. E., Westerström, R., Meuller, B. O., Blomberg, S., Gustafson, J., Andersen, J. N., et al. (2010). Generation of Pd model catalyst nanoparticles by spark discharge. *Journal of Physical Chemistry C, 114*(20), 9257–9263. https://doi.org/10.1021/jp101390a.

Park, J., Henins, I., Herrmann, H. W., Selwyn, G. S., Jeong, J. Y., Hicks, R. F., et al. (2000). An atmospheric pressure plasma source. *Applied Physics Letters*. https://doi.org/10.1063/1.125724.

Preger, C., Overgaard, N. C., Messing, M. E., & Magnusson, M. H. (2020). Predicting the deposition spot radius and the nanoparticle concentration distribution in an electrostatic precipitator. *Aerosol Science and Technology, 54*(6), 718–728. https://doi.org/10.1080/02786826.2020.1716939.

Reiprich, J., Gebinoga, M., Traue, L. P., Schlag, L., Biswas, S., Kaltwasser, M., et al. (2018). Localized collection of airborne biological hazards for environmental monitoring. *Sensors and Actuators B: Chemical*. https://doi.org/10.1016/j.snb.2018.06.129.

Rodríguez-Pérez, D., Castillo, J. L., & Antoranz, J. C. (2005). Relationship between particle deposit characteristics and the mechanism of particle arrival. *Physical Review E - Statistical, Nonlinear and Soft Matter Physics*. https://doi.org/10.1103/PhysRevE.72.021403.

Rusinque, H., Fedianina, E., Weber, A., & Brenner, G. (2019). Numerical study of the controlled electrodeposition of charged nanoparticles in an electric field. *Journal of Aerosol Science*. https://doi.org/10.1016/j.jaerosci.2018.11.005.

Sabzehparvar, M., Kiani, F., & Tabrizi, N. S. (2018). Spark discharge generation of superparamagnetic Nickel Oxide nanoparticles. *Materials Today: Proceedings, 5*(7), 15821–15827. https://doi.org/10.1016/j.matpr.2018.05.080. , Part 3.

Saporoschenko, M. (1965). Mobility of mass-analyzed N+, N 2+, N 3+, and N 4+ ions in nitrogen gas. *Physical Review, 139*, A352.

Sauerbrey, G. (1959). Verwendung von Schwingquarzen zur Wägung dünner Schichten und zur Mikrowägung. *Zeitschrift Für Physik, 155*(2), 206–222. https://doi.org/10.1007/BF01337937.

Schütze, A., Jeong, J. Y., Babayan, S. E., Park, J., Selwyn, G. S., & Hicks, R. F. (1998). The atmospheric-pressure plasma jet: A review and comparison to other plasma sources. *IEEE Transactions on Plasma Science*. https://doi.org/10.1109/27.747887.

Steinem, C., & Janshoff, A. (2007). Piezoelectric sensors volume. Techniques. https://doi.org/10.1007/b100321.

Tabrizi, N. S., Ullmann, M., Vons, V. A., Lafont, U., & Schmidt-Ott, A. (2009). Generation of nanoparticles by spark discharge. *Journal of Nanoparticle Research, 11*(2), 315–332. https://doi.org/10.1007/s11051-008-9407-y.

Tang, J., & Gomez, A. (2017). Controlled mesoporous film formation from the deposition of electrosprayed nanoparticles. *Aerosol Science and Technology*. https://doi.org/10.1080/02786826.2017.1303573.

Tendero, C., Tixier, C., Tristant, P., Desmaison, J., & Leprince, P. (2006). Atmospheric pressure plasmas: A review. Spectrochimica acta - Part B atomic spectroscopy. https://doi.org/10.1016/j.sab.2005.10.003.

Thornton, J. A. (1977). High rate thick film growth. Annual review of materials science. https://doi.org/10.1146/annurev.ms.07.080177.001323.

Vons, V. A., Leegwater, H., Legerstee, W. J., Eijt, S. W. H., & Schmidt-Ott, A. (2010). Hydrogen storage properties of spark generated palladium nanoparticles. *International Journal of Hydrogen Energy, 35*, 5479–5489. https://doi.org/10.1016/j.ijhydene.2010.02.118.

White, H. J. (1951). Particle charging in electrostatic precipitation. *Transactions of the American Institute of Electrical Engineers, 70*(2), 1186–1191. https://doi.org/10.1109/T-AIEE.1951.5060545.